Astron. Nachr. / AN **332**, No. 1, 43 – 50 (2011) / **DOI** 10.1002/asna.201012345

Dependence of the large-scale vortex instability on latitude, stratification and domain size

M.J. Mantere[1,⋆], **P.J. Käpylä**[1,2], **and T. Hackman**[1,3]

[1] Department of Physics, PO BOX 64 (Gustaf Hällströmin katu 2a), FI-00014 University of Helsinki, Finland
[2] NORDITA, AlbaNova University Center, Roslagstullsbacken 23, SE-10691 Stockholm, Sweden
[3] Finnish Centre for Astronomy with ESO, University of Turku, Väisäläntie 20, FI-21500 Piikkiö, Finland

Received 2011 Aug 31, accepted 2011 Nov 10
Published online 2012 Jan 12

Key words Hydrodynamics – convection – turbulence

In an earlier study, we reported on the excitation of large-scale vortices in Cartesian hydrodynamical convection models subject to rapid enough rotation. In that study, the conditions of the onset of the instability were investigated in terms of the Reynolds (Re) and Coriolis (Co) numbers in models located at the stellar North pole. In this study, we extend our investigation to varying domain sizes, increasing stratification and place the box at different latitudes. The effect of the increasing box size is to increase the sizes of the generated structures, so that the principal vortex always fills roughly half of the computational domain. The instability becomes stronger in the sense that the temperature anomaly and change in the radial velocity are observed to be enhanced. The model with the smallest box size is found to be stable against the instability, suggesting that a sufficient scale separation between the convective eddies and the scale of the domain is required for the instability to work. The instability can be seen upto the co-latitude of 30 degrees, above which value the flow becomes dominated by other types of mean flows. The instability can also be seen in a model with larger stratification. Unlike the weakly stratified cases, the temperature anomaly caused by the vortex structures is seen to depend on depth.

1 Introduction

Hydrodynamical Cartesian convection simulations subject to high enough rotational influence ($\mathrm{Co} \gtrsim 3$) and exhibiting large enough Reynolds number ($\mathrm{Re} \gtrsim 30$) have been reported to generate vortices, the sizes of which are large compared to the size of the convection cells (e.g. Chan 2003, 2007; Käpylä, Mantere & Hackman, 2011, hereafter KMH11). In the moderate Coriolis number regime, the vortices are cyclonic, suppressing the energy transport by convection, and thereby appearing as cooler than their surroundings. When Coriolis number is increased even further, anticyclonic vortices are preferred, enhancing the convective energy transport, making the vortices appear as regions warmer than their surroundings (KMH11).

In our previous study (KMH11), we proposed that such vortical structures could be responsible for cool/hot starspots in rapidly rotating late-type stars possessing outer convection zones. We were prompted to look into such a possibility due to the decorrelation of the surface temperature maps, obtained by Doppler-imaging techniques, from the distribution of surface magnetic fields, derived through Zeeman-Doppler imaging methods (e.g. Donati & Collier Cameron 1997; Donati 1999; Hussain et al. 2000; Jeffers et al. 2011; Kochukhov et al. 2011).

The resulting temperature anomaly due to the vortices was shown to be of the order of 5 percent, being somewhat weaker than the temperature contrasts deduced from observations. The model, however, was very simple: for example, the density stratification in the radial direction was only of the order of 23. Due to the low growth rate of the instability, requiring several thousand turnover times to saturate, only a very limited parameter range was studied. In this study, we extend the previous one by investigating a model with a larger stratification, models with varying domain size, and place the computational domains at different latitudes.

⋆ Corresponding author: maarit.mantere@helsinki.fi

2 Model

Our model is based on that used by Käpylä et al. (2009) and KMH11. A rectangular portion of a star is modeled by a box situated at colatitude θ. The box is divided into three layers: an upper cooling layer, a convectively unstable layer, and a stable overshoot layer (see below). We solve the following set of equations for compressible hydrodynamics:

$$\frac{\mathrm{D}\ln\rho}{\mathrm{D}t} = -\boldsymbol{\nabla}\cdot\boldsymbol{U}, \tag{1}$$

$$\frac{\mathrm{D}\boldsymbol{U}}{\mathrm{D}t} = -\frac{1}{\rho}\boldsymbol{\nabla}p + \boldsymbol{g} - 2\boldsymbol{\Omega}\times\boldsymbol{U} + \frac{1}{\rho}\boldsymbol{\nabla}\cdot 2\nu\rho\mathsf{S}, \tag{2}$$

$$\frac{\mathrm{D}e}{\mathrm{D}t} = -\frac{p}{\rho}\boldsymbol{\nabla}\cdot\boldsymbol{U} + \frac{1}{\rho}\boldsymbol{\nabla}\cdot K\boldsymbol{\nabla}T + 2\nu\mathsf{S}^2 - \frac{e-e_0}{\tau(z)}, \tag{3}$$

where $\mathrm{D}/\mathrm{D}t = \partial/\partial t + \boldsymbol{U}\cdot\boldsymbol{\nabla}$ is the advective time derivative, ν is the kinematic viscosity, K is the heat conductivity,

ρ is the density, $\boldsymbol{U}$ is the velocity, $\boldsymbol{g} = -g\hat{\boldsymbol{z}}$ is the gravitational acceleration, and $\boldsymbol{\Omega} = \Omega_0(-\sin\theta, 0, \cos\theta)$ is the rotation vector. The fluid obeys an ideal gas law $p = (\gamma-1)\rho e$, where p and e are the pressure and the internal energy, respectively, and $\gamma = c_{\rm P}/c_{\rm V} = 5/3$ is the ratio of the specific heats at constant pressure and volume, respectively. The specific internal energy per unit mass is related to the temperature via $e = c_{\rm V}T$. The rate of the strain tensor S is given by

$$\mathsf{S}_{ij} = \tfrac{1}{2}(U_{i,j} + U_{j,i}) - \tfrac{1}{3}\delta_{ij}\boldsymbol{\nabla}\cdot\boldsymbol{U}. \quad (4)$$

The last term of Eq. (3) describes the cooling at the top of the domain. Here $\tau(z)$ is a cooling time which has a profile smoothly connecting the upper cooling layer and the convectively unstable layer below, where $\tau \to \infty$.

The positions of the bottom of the box, bottom and top of the convectively unstable layer, and the top of the box, respectively, are given by $(z_1, z_2, z_3, z_4) = (-0.85, 0, 1, 1.15)d$, where d is the depth of the convectively unstable layer. In the case of larger stratification (Set C), the corresponding vertical positions read $(z_1, z_2, z_3, z_4) = (-0.4, 0, 1, 1.1)d$, resulting in a vertical extent somewhat smaller than in Sets A and D. Initially the stratification is piecewise polytropic with polytropic indices $(m_1, m_2, m_3) = (3, 1, 1)$, which leads to a convectively unstable layer above a stable layer at the bottom of the domain. In a system set up this way, convection transports roughly 20 per cent of the total flux. Due to the presence of the cooling term, a stably stratified isothermal layer forms at the top. The standard horizontal extent of the box, $L_{\rm H} \equiv L_x = L_y$, is $4d$; the horizontal domain size is varied from half of this to double the size in Set A. In Set C with larger stratification, the horizontal extent of the box is $5d$. The simulations in Sets A and C are made at the North pole, corresponding to $\theta = 0^\circ$, while in Set D, the co-latitude is varied with coarse steps to cover the latitude range down to $\theta = 60^\circ$. The simulations were performed with the PENCIL CODE[1], which is a high-order finite difference method for solving the compressible equations of magnetohydrodynamics.

2.1 Units and non-dimensional parameters

Non-dimensional quantities are obtained by setting

$$d = g = \rho_0 = c_{\rm P} = 1\,, \quad (5)$$

where ρ_0 is the initial density at z_2. The units of length, time, velocity, density, and entropy are

$$[x] = d\,,\ \ [t] = \sqrt{d/g}\,,\ \ [U] = \sqrt{dg}\,,$$
$$[\rho] = \rho_0\,,\ \ [s] = c_{\rm P}. \quad (6)$$

We define the Prandtl number and the Rayleigh number as

$$\mathrm{Pr} = \frac{\nu}{\chi_0}\,,\ \ \mathrm{Ra} = \frac{gd^4}{\nu\chi_0}\left(-\frac{1}{c_{\rm P}}\frac{{\rm d}s}{{\rm d}z}\right)_0\,, \quad (7)$$

where $\chi_0 = K/(\rho_{\rm m}c_{\rm P})$ is the thermal diffusivity, and $\rho_{\rm m}$ is the density in the middle of the unstable layer, $z_{\rm m} = \frac{1}{2}(z_3 - z_2)$. The entropy gradient, measured at $z_{\rm m}$, in the non-convective hydrostatic state, is given by

$$\left(-\frac{1}{c_{\rm P}}\frac{{\rm d}s}{{\rm d}z}\right)_0 = \frac{\nabla - \nabla_{\rm ad}}{H_{\rm P}}\,, \quad (8)$$

where $\nabla - \nabla_{\rm ad}$ is the superadiabatic temperature gradient with $\nabla_{\rm ad} = 1 - 1/\gamma$, $\nabla = (\partial \ln T/\partial \ln p)_{z_{\rm m}}$, and where $H_{\rm P}$ is the pressure scale height. The amount of stratification is determined by the parameter $\xi_0 = (\gamma-1)e_0/(gd)$, which is the pressure scale height at the top of the domain normalized by the depth of the unstable layer. We use $\xi_0 = 1/3$ in Sets A and B, which results in a density contrast of about 23 across the whole domain, and roughly 9 over the convectively unstable layer. We make one run with higher stratification (C1), for which $\xi_0 = 1/6$, resulting in a density contrast of roughly 230 over the convectively unstable layer. We define the Reynolds and Péclet numbers via

$$\mathrm{Re} = \frac{u_{\rm rms}}{\nu k_{\rm f}}\,,\ \ \mathrm{Pe} = \frac{u_{\rm rms}}{\chi_0 k_{\rm f}} = \mathrm{Pr}\ \mathrm{Re}\,, \quad (9)$$

where $k_{\rm f} = 2\pi/d$ is adopted as an estimate for the wavenumber of the energy-carrying eddies, and $u_{\rm rms} = \sqrt{3u_z^2}$. This definition of $u_{\rm rms}$ neglects the contributions from the large-scale vortices that are generated in the rapid rotation regime. Note that with our definitions Re and Pe are smaller than the usual ones by a factor of 2π. The amount of rotation is quantified by the Coriolis number, defined as

$$\mathrm{Co} = \frac{2\Omega_0}{u_{\rm rms}k_{\rm f}}\,. \quad (10)$$

We also quote the value of the Taylor number,

$$\mathrm{Ta} = \left(2\Omega_0 d^2/\nu\right)^2, \quad (11)$$

which is related to the Ekman number via $\mathrm{Ek} = \mathrm{Ta}^{-1/2}$.

2.2 Boundary conditions

The horizontal boundaries are periodic for all variables. Stress-free conditions are used for the velocity at the vertical boundaries.

$$U_{x,z} = U_{y,z} = U_z = 0. \quad (12)$$

The temperature is kept constant on the upper boundary and the temperature gradient

$$\frac{dT}{dz} = \frac{-g}{c_{\rm V}(\gamma-1)(m+1)}, \quad (13)$$

is held constant at the lower boundary, yielding a constant heat flux $F_0 = -K\partial T/\partial z$ through the lower boundary.

3 Results

In an earlier study, we investigated the excitation of large-scale vortices in Cartesian domains with weak density stratification, located at the North pole of a rapidly rotating star (KMH11). In that study, we investigated the limiting Reynolds and Coriolis numbers (i.e. inverse Rossby numbers) above which the instability was excited. For the

[1] http://code.google.com/p/pencil-code/

Run	grid	$L_{\rm H}$	θ	$\Delta\rho$	$T_{\rm cyc}/\overline{T}$	Re	Pe	Pr	Ra	Co	Ta	$\tilde{F}_0$	Cyc.
D1	$256^2 \times 128$	1	60	9	-	47	23	0.48	$2.0 \cdot 10^6$	5.3	$1.0 \cdot 10^8$	$1.7 \cdot 10^{-5}$	no
D2	$256^2 \times 128$	1	45	9	-	43	20	0.48	$2.0 \cdot 10^6$	5.9	$1.0 \cdot 10^8$	$1.7 \cdot 10^{-5}$	no
D3*	$256^2 \times 128$	1	30	9	-	47	23	0.48	$2.0 \cdot 10^6$	5.4	$1.0 \cdot 10^8$	$1.7 \cdot 10^{-5}$	yes (A+C)
D4*	$256^2 \times 128$	1	15	9	-	44	21	0.48	$2.0 \cdot 10^6$	5.8	$1.0 \cdot 10^8$	$1.7 \cdot 10^{-5}$	yes (A+C)
D5*	$256^2 \times 128$	1	0	9	-	45	22	0.48	$2.0 \cdot 10^6$	5.6	$1.0 \cdot 10^8$	$1.7 \cdot 10^{-5}$	yes (C)
A1*	$512^2 \times 128$	2	0	9	(0.099)	42	15	0.36	$2.0 \cdot 10^6$	8.1	$1.8 \cdot 10^8$	$1.7 \cdot 10^{-5}$	yes ($2 \times$ A)
A2	$256^2 \times 128$	1	0	9	0.045	44	16	0.36	$2.0 \cdot 10^6$	7.7	$1.7 \cdot 10^8$	$1.7 \cdot 10^{-5}$	yes (A)
A3	$128^2 \times 128$	0.5	0	9	-	39	14	0.36	$2.0 \cdot 10^6$	8.7	$1.8 \cdot 10^8$	$1.7 \cdot 10^{-5}$	no
C1*	$256^2 \times 192$	1	0	233	(0.052)	94	48	0.5	$1.3 \cdot 10^7$	4.3	$2.6 \cdot 10^8$	$3.4 \cdot 10^{-5}$	yes (A+C)

Table 1 Summary of the runs. Stars indicate that the simulation has not been run to a saturated state. The amount of stratification, $\Delta\rho$, is measured over the convectively unstable region. The temperature anomaly, $T_{\rm cyc}/\overline{T}$, where $T_{\rm cyc}$ is the extremum of temperature in a cyclonic region and $\overline{T}$ the mean temperature of certain horizontal layer, is measured at the middle of the convective layer, z_m. The dimensionless input heat flux at the lower boundary of the box is given by $\tilde{F}_0 = F_0/(\rho c_{\rm s}^3)$, where $c_{\rm s}$ is the adiabatic sound speed and ρ is the density, both measured at the lower boundary of the domain. The last column indicates the presence of cyclonic (C), anti-cyclonic (A), or both types (A+C) of vortices.

present study, we have extended our analysis to models with varying computational domain size (Sect. 3.1), place the box at different latitudes of the star (Sect. 3.2), and present a model with higher density stratification (Sect. 3.3). The most relevant input parameters for the runs and some essential output quantities are listed in Table 1. As is evident from this table, some of the runs generating vortices have not yet reached a completely saturated state (these runs are marked with stars), even though they have been integrated for several thousands of turnover times. In such cases, quantities such as the temperature anomaly between the vortex and its surroundings, might still be underestimated, and the listed numbers in Table 1 should be regarded as lower limits.

3.1 Dependence on the domain size

In our previous computations with the standard box size of $L_{\rm H}$=4d (KMH11), we observed a clear tendency of the sizes of the vortices to approach the wavenumber k/k_1=1, i.e. they tended to fill in as large a fraction of the horizontal extent as possible. This prompted us to study the dependence of the instability on the horizontal extent of our Cartesian box. In Run A3 of this paper (see Table 1), both the horizontal extent and resolution of the domain are halved. Run A2 is a model with the standard box sixe (actually otherwise identical to D5 except for the value of the kinematic viscosity), and in Run A3 the resolution and horizontal extent are doubled. In all the runs, the computational domain is located at the North pole of the star.

In Run A3, the Reynolds (roughly 39) and Coriolis numbers (roughly 8.7) are clearly above the critical values found in KMH11; still, no vortices are excited. This is evident from the leftmost panels of Fig. 1, where we show the temperature field (upper panel) and radial velocity (lower panel) at the middle of the convectively unstable layer, $z_{\rm m}$. Some large-scale $k/k_1 = 1$ pattern can be detected in the temperature field, that might be indicative of the early stages of the vortex-instability. This run, however, was continued up to 6500 turnover times, matching the timepoint of the slice plotted in Fig. 1. It is not completely ruled out that a very slowly growing vortex instability mode is present, but in any case its growth rate is strongly reduced from the standard box runs presented in KMH11.

Run A2 shows very similar behavior to the earlier calculations presented in KMH11: the Reynolds number is clearly supercritical to the instability (roughly 44), and Coriolis number (roughly 7.7) in the regime where the excitation of an anti-cyclone, i.e. a vortex rotating in opposite direction to the overall rotation of the domain, was reported. As shown in the middle panels of Fig. 1, a vortex rotating in the clock-wise direction is seen in the velocity field (lower panel), the structure being warmer than its surroundings (upper panel). The temperature anomaly is slightly less than five percent, very close to the number reported in KMH11. The temperature across the vortex, normalised to the mean temperature of the horisontal layer, is plotted in the upper panel of Fig. 2 with a red, dashed line. In the region of the anti-cyclone, the vertical velocities become somewhat enhanced, as evident from the lower panel of the same figure, where the velocity profile normalised to the rms velocity of the horisontal layer across the vortex is plotted with a red, dashed line.

In the model with the largest horizontal extent, Run A1, exhibiting very similar Reynolds and Coriolis numbers in comparison to the standard box Run A2, two instead of one anticyclones are seen. The growth rate of the instability, measured from the growth of the horizontal velocity components, increases by a factor of 2.3 from Run A2 to A1. As evident from the rightmost panels of Fig. 1, the two structures are of unequal strength, possibly suggesting that the system has not yet completely saturated, although it has been followed for up to nearly 3000 turnover times. Based on earlier experience with the standard box runs (KMH11), where multiple vortices were also seen, when followed long enough, only one vortex very close to the k/k_1=1 wavenumber would be the stable end point for this value of Co.

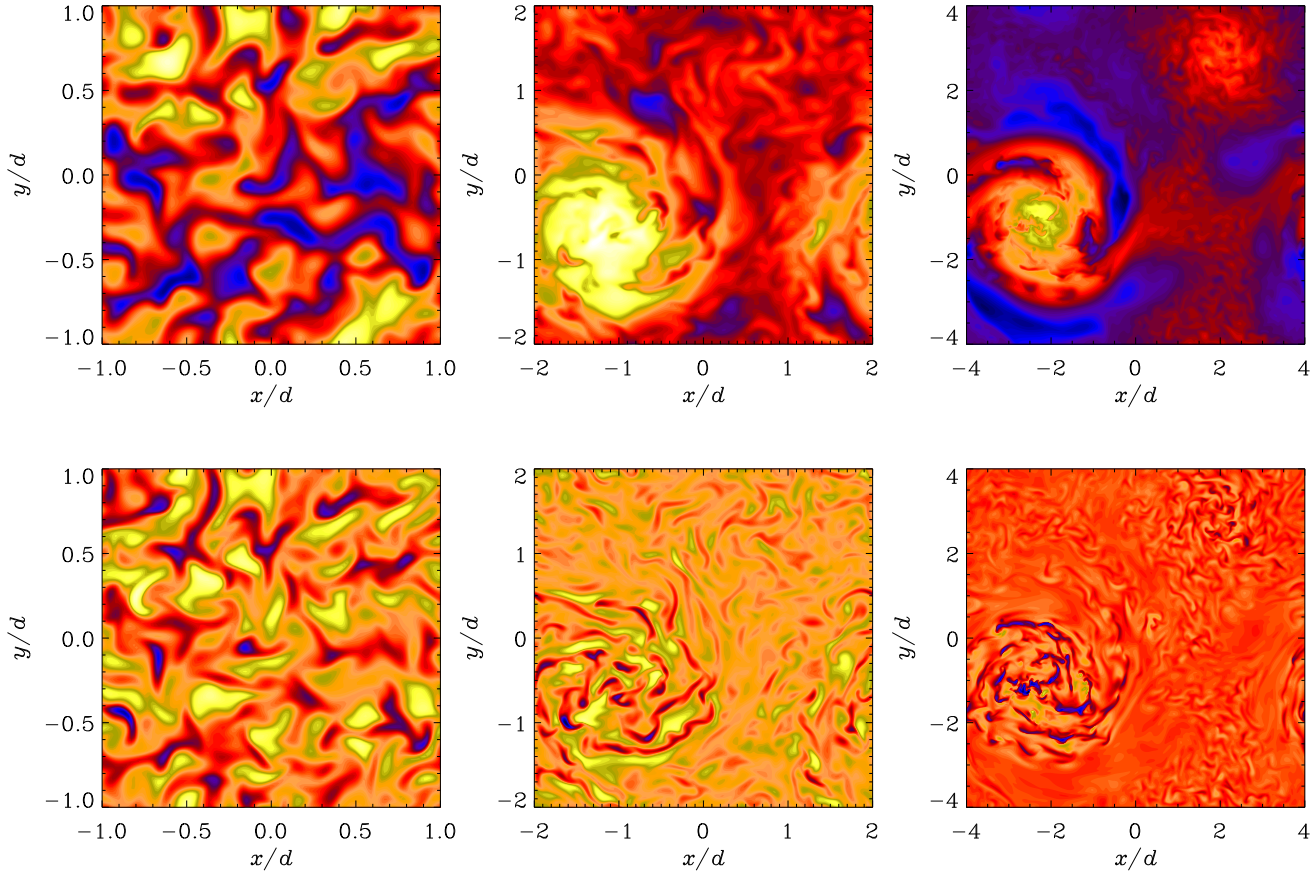

Fig. 1 Temperature (upper row) and radial velocity U_r (lower row) in the middle of the convectively unstable layer, i.e. at z_m, for Runs A3, A2 and A1 (from left to right). For Run A3, the slice is taken from the time $t = 6400\tau_\mathrm{to}$, where $\tau_\mathrm{to} = (u_\mathrm{rms}k_\mathrm{f})^{-1}$. For Runs A2 and A1, the snapshots are taken at $3400\tau_\mathrm{to}$ and $2700\tau_\mathrm{to}$.

The temperature and vertical velocity anomaly across the stronger vortex is plotted in Fig. 2 with solid, black lines. As can be seen from this figure, the heating effect in the middle of the vortex is roughly twice as large as in the standard box case, suggesting that the strength of the instability is indeed dependent on the box size. No such dramatic difference can be seen in the vertical velocity cut across the vortex (Fig. 2 lower panel).

The size of the stronger vortex in Run A1, again, is nearly half of the domain size, i.e. approaching the k/k_1=1 mode. In Fig. 3 we plot the power spectra for the kinetic energy from Runs A1 (black lines) and A2 (red lines); the wavenumber scale for Run A1 is re-scaled to match the one of Run A2. In the early stages, when no vortices are yet excited (dashed linestyles), both the power spectra consistently peak at intermediate wavenumber of roughly k/k_1=7; this number reflects the size of the turbulent eddies due to convective motions. Due to the appearance of the vortices, the energy contained in large scales grows, and dominates the flow in the nearly saturated stage. Most of the power is seen near the wavenumber k/k_1=1. In Run A1, the instability would still have 'space' to advance into even lower wavenumbers i.e. larger scales; followed up even further, it might still do so.

3.2 Latitudinal dependence

In Set D, we place the computational domain at different co-latitudes with a very coarse latitude grid of $[0, 15, 30, 45, 60]$ using the standard box size. In all the runs in Set D, the Reynolds and Coriolis numbers are kept above the critical values found by KMH11. In Runs D5, D4 and D3, we still observe the excitation of vortices, but in the rest, other types of large-scale flows are generated, suppressing the instability. Such large-scale flows are normally referred to as banana cells, seen both in Cartesian (Chan 2001; Käpylä et al. 2004) and spherical geometries (e.g. Brown et al. 2008; Käpylä et al. 2011a, 2011b).

The structures extend through the whole convection zone and even penetrate to the overshoot region, see Fig. 4, where we plot a radial-vertical (xz) slice of the azimuthal velocity U_y from Run D3 with θ=30°. The convection and also the vortex tube, are strongly affected by rotation, which forces the structures to become inclined with the axis of rotation.

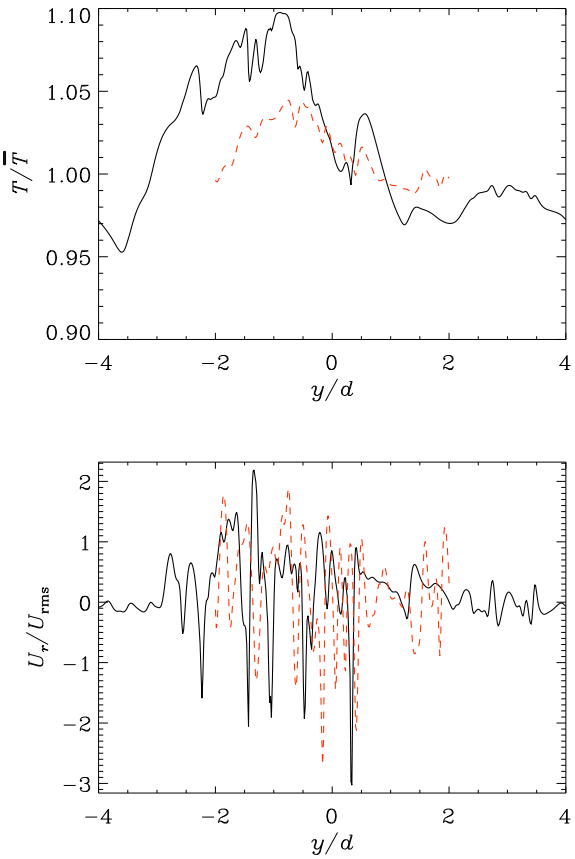

Fig. 2 Temperature (upper panel) and vertical velocity U_r (lower panel) across the anticyclone for Runs A1 and A2 with differing box size.

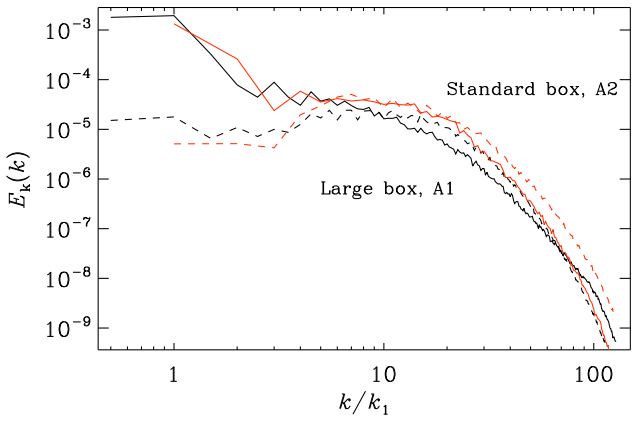

Fig. 3 Kinetic energy spectra for the Runs A1 (black lines) and A2 (red lines). Spectra taken at early times, when no vortices are yet excited, are plotted with dashed linestyle, and spectra from the vortex-state with solid linestyle. The wavenumber range of Run A1 is scaled to match the one of Run A2.

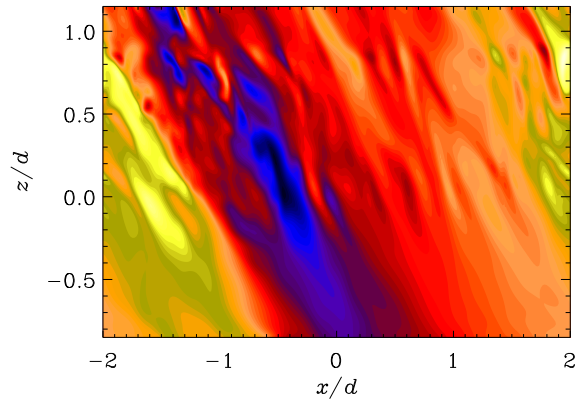

Fig. 4 Two-dimensional slice, in the xz-plane, of the azimuthal velocity U_y from the run D3 at co-latitude 30 degrees. The anticyclone generated in the run shows up as a structure spanning through the entire vertical extent of the computational domain, inclined with the rotation vector.

The growth rate of the instability is reduced when the co-latitude is increased; therefore, it has been extremely difficult to follow the Runs D3 and D4 up to saturation. The run at the pole (D5) having the largest growth rate has been run to a state very near saturation, when the growth of the horizontal velocity components slows down. In an earlier state, this run also exhibited both an anti-cyclonic and cyclonic vortex; in the later stages, however, only the cyclone persists. The other runs still show both types of vortices, but this may still change as these runs are relatively further away from the saturated state in comparison to D5.

3.3 Dependence on stratification

We have made an attempt to quantify the effect of increasing stratification on the vortex instability by running one model where the stratification is almost 30 times larger than in our standard cases. Due to this, larger resolution in the radial direction is needed; the amount of gridpoints has been increased from nz=128 to 192, making these computations even more demanding than the rest included in this study. This run is identified as Run C1 in Table 1, and can be observed to have a much higher Reynolds number (roughly 94) than any other run, but clearly a lower Coriolis number (roughly 4.3) than the rest of the runs. Nevertheless, these numbers exceed the critical values found in KMH11, and therefore the vortex-instability is to be expected, unless the increased stratification has a significant effect on its excitation conditions.

Indeed, we observe the instability in Run C1, generating a stronger cyclonic and a weaker anti-cyclonic vortex, although the growth rate of it is reduced in comparison to the other runs due to the lower Coriolis number. We have been able to calculate this model up to roughly 2000 turnover times, but it is clear that the system is still

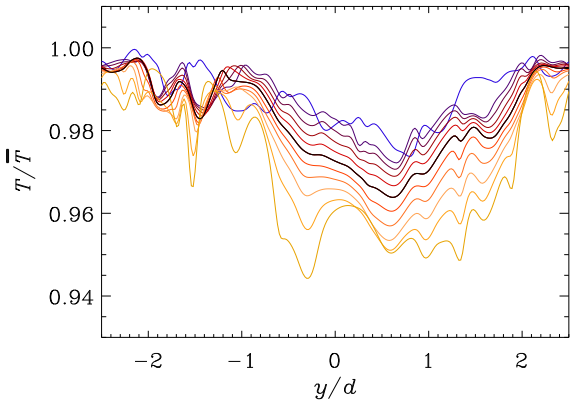

Fig. 5 Azimuthal cuts through the computational domain at $x = -1.1$ for various depths. The bluer the color, the nearer the bottom of the convection zone the cut is taken. Red colors represent cuts near $z_{\rm m}$, and the black line a cut taken exactly at $z_{\rm m}$. The yellow colors represent cuts taken near the top of the convection zone.

far from saturation. Nevertheless, the temperature anomaly measured at this relatively early stage is already comparable (maximally close to 5%) to the standard box calculations very near saturation. The vortices, again, occur at the very largest scales of the box, and their size does not vary significantly as a function of depth, even though the system is more strongly stratified. The temperature anomaly, on the contrary, varies monotonically through the convection zone, see Fig. 5, where we plot a temperature cut in the y-direction through a cyclonic, cooler, region located at $x = -1.1$ for various depths. From this figure it is evident that the temperature contrast is monotonically increasing as function of depth. In the models with weaker stratification, such an effect is not clearly visible.

4 Conclusions

In an earlier study (KMH11) we reported on the excitation of large-scale vortices in Cartesian hydrodynamical convection models subject to rapid enough rotation. In that study, the conditions of the onset of the instability were investigated in terms of the Reynolds and Coriolis numbers in models located at the stellar North pole. In this study, we extend our investigation to varying domain sizes, increasing stratification and place the box at different latitudes.

The effect of the increasing box size is to increase the sizes of the generated structures, so that the principal vortex always fills roughly half of the computational domain. The instability becomes stronger in the sense that the temperature anomaly and change in the radial velocity are observed to be enhanced. Also the growth rate, measured from the time evolution of the horizontal velocity components, is more than doubled when the boxsize is doubled. The model with the smallest box size is found to be stable against the instability even though the critical Reynolds and Coriolis numbers found in the earlier study KMH11 are clearly exceeded, suggesting that a sufficient scale separation between the convective eddies and the smallest wavenumber of the domain is required for the instability to work.

The instability can be seen up to a co-latitude of 30 degrees, but at higher co-latitudes, the flow becomes dominated by large-scale flows known as banana cells. Such flows have earlier been found from Cartesian and spherical convection models. The vortices are seen to align with the rotation vector, forming structures tilted but coherent through the entire convection zone, extending even to the overshoot region. The growth rate of the instability is observed to become lower with increasing co-latitude.

Only very little variance of the temperature contrast across the vortices can be seen as function of depth when stratification is small. The instability can also be seen in a model with larger stratification. Unlike the weakly stratified cases, the temperature anomaly caused by the vortex sturctures is seen to depend on depth.

Acknowledgements. Computational resources granted by CSC – IT Center for Science, who are financed by the Ministry of Education, and financial support from the Academy of Finland grants No. 136189, 140970 (PJK) and 218159, 141017 (MJM), and the 'Active Suns' research project at University of Helsinki (TH) is acknowledged. The authors acknowledge the hospitality of NORDITA during their visits.

References

Brown, B.P., Browning, M.K., Brun, A.S., Miesch, M.S., Toomre, J.: 2008, ApJ 689, 1354
Chan, K. L. 2001, ApJ, 548, 1102
Chan, K. L. 2003, in Astronomical Society of the Pacific Conference Series, Vol. 293, 3D Stellar Evolution, ed. S. Turcotte, S. C. Keller, & R. M. Cavallo, 168
Chan, K. L. 2007, AN, 328, 1059
Donati, J.-F. 1999, MNRAS, 302, 457
Donati, J.-F., & Collier Cameron, A. 1997, MNRAS, 291, 1
Hussain, G. A. J., Donati, J.-F., Collier Cameron, A., & Barnes, J. R. 2000, MNRAS, 318, 961
Jeffers, S. V., Donati, J.-F., Alecian, E., & Marsden, S. C. 2011, MNRAS, 411, 1301
Käpylä, P. J., Korpi, M. J., Tuominen, I. 2004, A&A, 422, 793
Käpylä, P. J., Korpi, M. J., & Brandenburg, A. 2009, ApJ, 697, 1153
Käpylä, P. J., Mantere, M. J. & Hackman, T., 2011, ApJ (in press), arXiv:1106.6029
Käpylä, P. J., Mantere, M. J., Brandenburg, A., 2011b, AN, submitted
Käpylä, P. J., Korpi, M. J., Guerrero, G., Brandenburg, A., Chatterjee, P. 2011a, A&A, 531, A162
Kochukhov, O., Hackman, T., Mantere, M. J., Ilyin, I., Piskunov, N., & Tuominen, I. 2011, In preparation

